In Situ Quantitative Tensile Testing of Antigorite in a Transmission Electron Microscope

Hosni Idrissi[1,2] , Vahid Samaee[2] , Gunnar Lumbeeck[2], Thomas van der Werf[1,2], Thomas Pardoen[1], Dominique Schryvers[2] , and Patrick Cordier[3,4]

[1]Institute of Mechanics, Materials and Civil Engineering, UCLouvain, Louvain-la-Neuve, Belgium, [2]Electron Microscopy for Materials Science, University of Antwerp, Antwerp, Belgium, [3]Univ. Lille, CNRS, INRAE, Centrale Lille, UMR 8207-UMET-Unité Matériaux et Transformations, Lille, France, [4]Institut Universitaire de France, Paris, France

Abstract The determination of the mechanical properties of serpentinites is essential toward the understanding of the mechanics of faulting and subduction. Here we present the first in situ tensile tests on antigorite in a transmission electron microscope. A push-to-pull deformation device is used to perform quantitative tensile tests, during which force and displacement are measured, while the evolving microstructure is imaged with the microscope. The experiments have been performed at room temperature on $2 \times 1 \times 0.2$ μm^3 beams prepared by focused ion beam. The specimens are not single crystals despite their small sizes. Orientation mapping indicated that several grains were well oriented for plastic slip. However, no dislocation activity has been observed even though the engineering tensile stress went up to 700 MPa. We show also that antigorite does not exhibit a purely elastic-brittle behavior since, despite the presence of defects, the specimens accumulate permanent deformation and did not fail within the elastic regime. Instead, we observe that strain localizes at grain boundaries. All observations concur to show that under these experimental conditions, grain boundary sliding is the dominant deformation mechanism. This study sheds a new light on the mechanical properties of antigorite and calls for further studies on the structure and properties of grain boundaries in antigorite and more generally in phyllosilicates.

1. Introduction

Serpentinites form by hydrothermal alteration of ultramafic rocks (dunite, peridotite, and pyroxenite) at low (100 °C) to intermediate (700 °C) temperature. Containing up to 13% water in weight (structural formula of serpentine minerals: $Mg_3Si_2O_5(OH)_4$), serpentines are considered to play an important role in the global water cycle providing a possible path to entrain water at great depths in subduction zones (Scamberulli et al., 1995; Ulmer & Trommsdorff, 1995). Serpentinites represent only 3% to 4% of the Earth's surface; however, they are present at plate boundaries, for example, in transform faults or subducting slabs, where deformation is localized along centimeter- to kilometer-scale shear zones (e.g., Guillot & Hattori, 2013). Hence, their rheological properties have attracted a lot of attention, further triggered by a very peculiar crystal chemistry. The structural unit of serpentines is made of layers of Mg-rich trioctahedral sheet (O) attached to a single tetrahedral silicate sheet (T). Depending on the misfit between the larger T and O sheets, the layers are locally either flat (lizardite) or curved (antigorite and chrysotile). In antigorite, the periodic reversal of the T sheet along the *a* axis results in a curvy, modulated structure with in-plane covalent Si-O bonds. This periodic reversal prevents the formation of a tubular structure as in chrysotile. Phyllosilicates are usually considered as relatively weak materials; however, these structural differences potentially suggest contrasted mechanical properties. Indeed, antigorite lacks easy cleavage planes and exhibits a higher strength than lizardite and chrysotile (Amiguet et al., 2012, 2014).

The discovery in the 1960s of serpentinites at the Atlantic sea floor (Aumento & Loubat, 1971) has attracted a lot of interest for serpentinites and in particular for their mechanical properties. The pioneering work of Raleigh and Paterson (1965) confirmed experimentally that an antigorite-bearing serpentinite, "with ultimate strength comparable to that of granite at room temperature, showed a marked weakening above 500–600 °C." Even though several studies have been conducted since that, the rheology of antigorite is still incompletely understood. The recent survey of experimental results by Reynard (2013) suggests a prominent influence of pressure (see Figure 6 in Reynard, 2013). Below approximately 1 GPa, antigorite displays a ductile frictional behavior (Guillot et al., 2015). Escartin et al. (1997) emphasize the importance of nondilatant

brittle deformation in this regime by shear microcracking with no strong evidence for intragranular crystal plastic deformation. This conclusion is further supported by the recent study of David et al. (2018). At higher pressure, up to 4 GPa, Hilairet et al. (2007) report a power law rheology (stress exponent 3) and microstructures indicative of distributed and, to some extent, intracrystalline deformation. However, Auzende et al. (2015) showed that semibrittle mechanisms dominate at laboratory strain rates, even under confining pressure. In between (1–2 GPa) there seems to be a transitional regime with a combination of ductile and brittle processes (Chernak & Hirth, 2010). The main current issue is related to the need of extrapolating rheological laws determined at laboratory strain rates to natural strain rates. For this purpose, active deformation mechanisms must be compared in experimental and naturally deformed specimens. Crystallographic preferred orientations can provide information about strain history of natural samples. Antigorite serpentinites from different geological settings have been characterized by this technique. Some have been interpreted as resulting from dislocation creep involving various slip systems (Auzende et al., 2015; Bezacier et al., 2010; Brownlee et al., 2013; Katayama, 2009; Padrón-Navarta et al., 2012; Soda & Wenk, 2014), although the relationship with well-established intracrystalline deformation mechanisms is still poorly understood (Auzende et al., 2006, 2015). Other interpretations can be considered, however, like inherited textures from topotactic transformation (Boudier et al., 2010; Morales et al., 2013; Plümper et al., 2012). Andreani et al. (2005) and Wassmann et al. (2011) rather highlight the role played by fluids enhancing dissolution-precipitation creep.

A better understanding of the deformation mechanisms at play in antigorite is clearly needed to assess the validity of the rheological laws used to fit the experimental data. In particular, there are very few studies devoted to unraveling the deformation mechanisms by transmission electron microscopy (TEM). It is the aim of the present study to fill this gap by presenting the first in situ, room temperature, deformation experiments of antigorite in order to identify active deformation mechanisms.

2. Materials and Methods

2.1. Materials

2.1.1. Sample 624-10

Sample 624-10 has been collected from the Viso Mozzo unit in the Monviso eclogitic massif (Western Alps, Italy) and described in Auzende et al. (2006). This unit has undergone eclogitic facies P,T conditions (25 kbar and 525 ± 50 °C) in Angiboust et al. (2011).

2.1.2. Sample Cu65

Sample Cu65 has been collected in a serpentinite lens from a metamorphic unit from the Escambray Massif in Central Cuba. It has been described in Auzende et al. (2002). This metamorphic unit also recorded eclogitic facies conditions with pressure conditions of ≥ 12 kbar and temperature of ≥ 450 °C.

2.2. Methods

Sample Preparation. Suitable areas were selected on the petrographic thin sections, and a Helios Nanolab 650 dual beam FIB (focused ion beam)/SEM (scanning electron microscope) instrument was used to cut TEM sections of about $8 \times 4 \times 0.4$ μm^3. These TEM specimens were examined using bright-field TEM (BF-TEM) and selected area electron diffraction in a Tecnai G2 TEM operating at 200 kV. An area of around 4×1 μm^2 was selected from the FIB foil, which was cut again in the FIB/SEM and was then moved to a push-to-pull (PTP) device (Idrissi et al., 2016; Samaee et al., 2018) using an Omniprobe micromanipulator (Figures 1a and 1b). The uniaxial tension specimens were then attached to the PTP device using electron beam-deposited Pt and were further reduced in size to about $2 \times 1 \times 0.4$ μm^3 to create the "dog bone" shape as shown in Figure 1c. An ion beam of 2 kV/0.2 nA was employed to achieve the final thinning of the specimen on the PTP to a thickness around 200 nm and to minimize irradiation damage generated during high-voltage FIB thinning and mounting on both sides of the specimen.

In Situ TEM Nanomechanical Testing. The in situ uniaxial tension experiments were conducted in a FEI-Osiris operating at 200 kV using the conductive diamond flat puncher indenter of a single-tilt PI 95 TEM PicoIndenter (Bruker.Inc). On the PTP device (Figure 1a), four identical springs are distributed symmetrically at the corners. Therefore, when compression is applied to the semicircular end of the PTP device it results in tensile loading on the specimen attached across the gap in the middle of the device. In order to ensure homogeneous applied stress during the in situ tests, the specimens were mounted parallel to the tensile direction. The experiments were performed using the load control mode. Applied force on the specimen
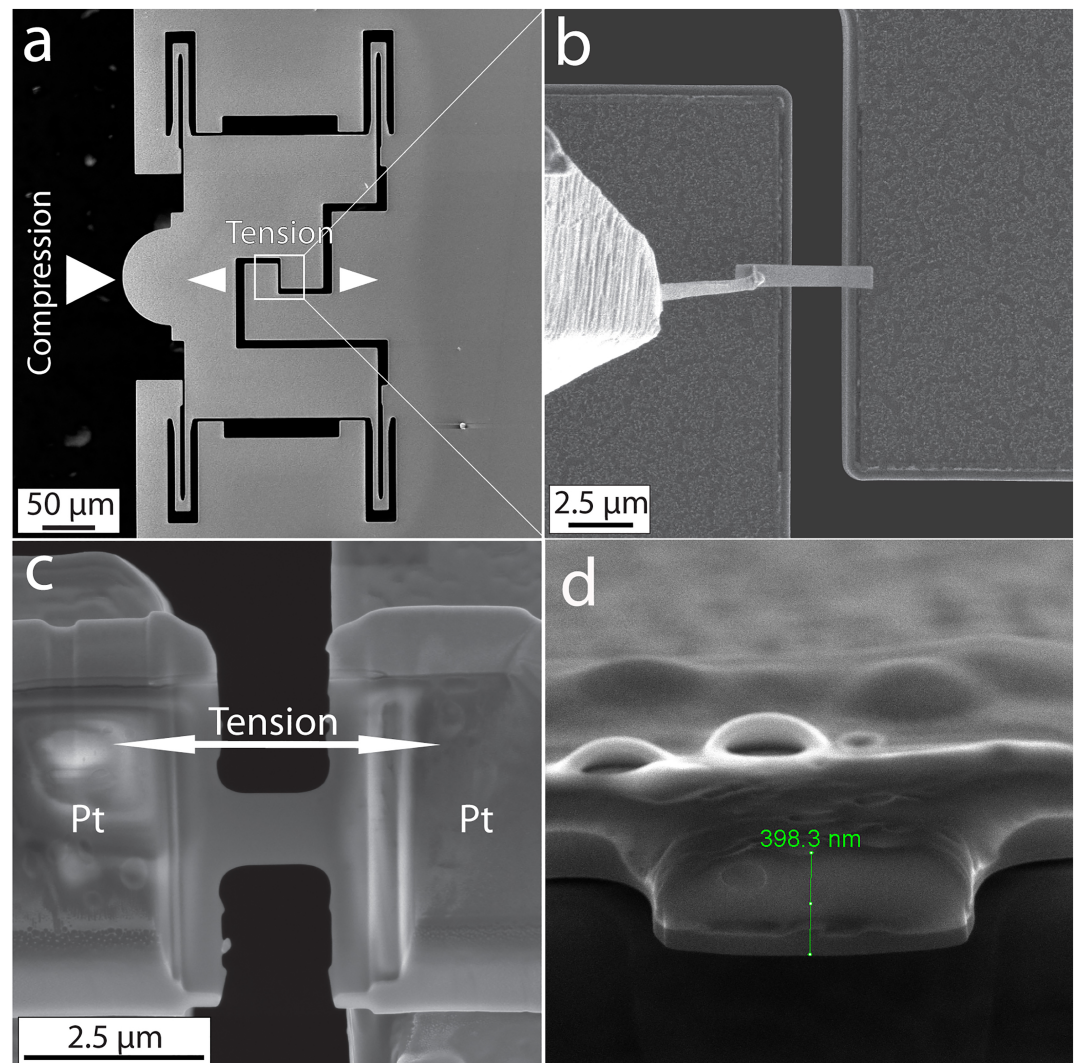
Figure 1. In situ TEM nanomechanical testing (a) optical image of the PTP device used for quantitative in situ TEM tensile experiments. The compression, with the diamond flat puncher indenter, of the semicircular end on the left opens the middle gap shown in (b) and (c), inducing uniaxial tension in the test specimen; (b) scanning electron microscope (SEM) image showing the transfer of a FIB-prepared specimen onto the PTP device; (c) SEM image showing the specimen mounted in the middle gap using electron beam-deposited platinum (Pt); (d) SEM measurements of the cross-sectional area of the tensile test specimen after fracture. Two antigorite samples (Ant624-10 and AntCu65) have been used to prepare the in situ TEM specimens; see section 2 for more details.

was determined by removing the contribution of the spring stiffness from the raw force. The engineering stress was calculated by dividing the force on the specimen by the cross-sectional area of the specimen. In order to perform accurate measurements of the cross-sectional area of the specimens, FIB has been used to remove the freestanding gage section (Figure 1c) after fracture. Then, the PTP device was mounted in the SEM chamber in such a way that the electron beam is almost perpendicular to the cross-sectional area of the tensile specimen (Figure 1d). Using this method, the cross-sectional area is accurately measured on the remaining nondeformed gage section attached with Pt (i.e., the two attachment points of the tensile test). The strain was determined by measuring the frame-by-frame displacement on the recorded TEM videos (using digital image correlation) and dividing this by the initial gage length (Chisholm et al., 2012; Idrissi et al., 2016; Samaee et al., 2018).

ACOM-TEM Analysis. The orientation maps of the antigorite specimens were generated by automated crystal orientation mapping in TEM (ACOM-TEM). This was performed in the Tecnai G2 TEM operating at 200 kV equipped with the ASTAR system from Nanomegas. The electron probe size was ~1.5 nm.

Electron precession was used with an angle of 0.4° to minimize dynamical effects. The data were posttreated with the orientation imaging microscopy analysis software from EDAX. In the ASTAR system, electron diffraction spot patterns are indexed (providing the local crystal orientations) by comparing individually obtained patterns via cross-correlation matching techniques with precalculated electron diffraction templates generated every 0.5° (orientation resolution). For antigorite, templates have been generated from the crystallographic data of Capitani and Merlini (2004) where the $m = 17$ polysome is described with monoclinic symmetry (Pm space group) with $a = 4.3505$ nm, $b = 0.9251$ nm, and $c = 0.7263$ nm.

3. Results

3.1. Ant624-10-01 Experiment

Figure 2a shows a BF-TEM image of a tensile specimen of ant624-10, mounted on the PTP device prior to deformation. The area of the specimen was preselected in the TEM in order to have the grain boundaries making an angle near 45° with the tensile axis. Figure 2a indicates that the grains exhibit an elongated morphology and a small size (from 100 to 400 nm). Some grains well oriented for Bragg reflection exhibit a high density of nanoscale thin parallel lamellae (twins and/or stacking faults) parallel to the basal plane (see the white arrowheads in Figure 2a). Two contrasts interpreted as dislocations indicated by D1 and D2 can also be observed in the same figure. Note that the nonsharp contrast of these defects is due to the presence of planar defects in the same region and to the fact that the grain is oriented close to Bragg conditions. Note also that the nonavailability of the double-tilt option in the picoindentor holder makes fine-tuning of dislocation contrast often very difficult.

Figure 2b exhibits both orientation and grain boundary (GB) maps in the region delimited by the red rectangle in Figure 2a (see supporting information for the reliability map). In this figure, low-angle GBs are defined by a misorientation angle smaller than 15°. The microstructure of the specimen in Figure 2b is dominated by grains oriented with directions normal to the figure plane nearly parallel to [100] or [010]. Figure 2d also provides the Schmid factors associated with the slip systems that have been experimentally reported for antigorite in the literature (i.e., $[100](001)$, $[010](001)$, $[101](10\overline{1})$, and $[10\overline{1}](101)$) (Amiguet et al., 2014; Bezacier et al., 2010; Brownlee et al., 2013). These values confirm that several domains are well oriented for plastic slip in all these systems with Schmid factors of the order of 0.4 to 0.5. Five deformation cycles were imposed under load control mode with a loading rate of 0.25 μN/s. Figure 2e exhibits the engineering stress-strain response for each cycle. After each cycle, the experiment was stopped in order to set the parameters of the following cycle. The maximum load was increased after each cycle. An apparent Young's modulus of 42.5 GPa (Table 1) was determined during loading using the slope from zero strain to the point at which a deviation from the initial linear regime is detected. No significant variation of the modulus between cycles was observed (see supporting information for more details). Since deformation is monitored in situ, the longitudinal and transverse strains can be simultaneously measured. Their ratio gives an apparent Poisson ratio equal to 0.20 (Table 1). Fracture occurs during the fifth cycle at an applied stress of 786 MPa and a total accumulated strain of 3.5% (Figure 2c). Fracture occurred along the two GBs indicated by dark arrowheads in Figure 2b, involving misorientation angles of 15° and 20°. Figure 2e shows that plastic deformation accumulates during the first four cycles as evidenced by the deviation from the pure elastic regime detected at an applied stress of ∼210 MPa for Cycle 1, 230 MPa for Cycles 2 and 3, 240 MPa for Cycle 4, and 270 MPa for Cycle 5 (see also Movie Ant624-10-01-Cycle4 at https://doi.org/10.5281/zenodo.3583135). Furthermore, a slight increase of strain occurs at the beginning of unloading, indicating some minor creep contribution. However, despite the high Schmid factor in several grains, no evidence of intragranular plasticity involving dislocation motion was detected in all the analyzed movies. This is in agreement with the observation of the absence of glide of the two dislocations D1 and D2 in grain 12 of Figure 2b when comparing the specimen before deformation (Figure 2a) and after fracture (Figure 2c). These results point toward a pivotal role of intergranular plasticity mechanisms that will be confirmed in the following sections.

3.2. AntCU65-01 Experiment

A BF-TEM micrograph as well as an ACOM-TEM map of a tensile specimen of AntigoriteCU65 before deformation are shown in Figures 3a and 3b, respectively. Similarly to the previous specimen, stacking defects parallel to the basal plane can be clearly identified (black arrowheads in Figure 3a). Furthermore, a few nanocracks can be observed (white arrowheads in Figure 3a). The determination of the Schmid factors
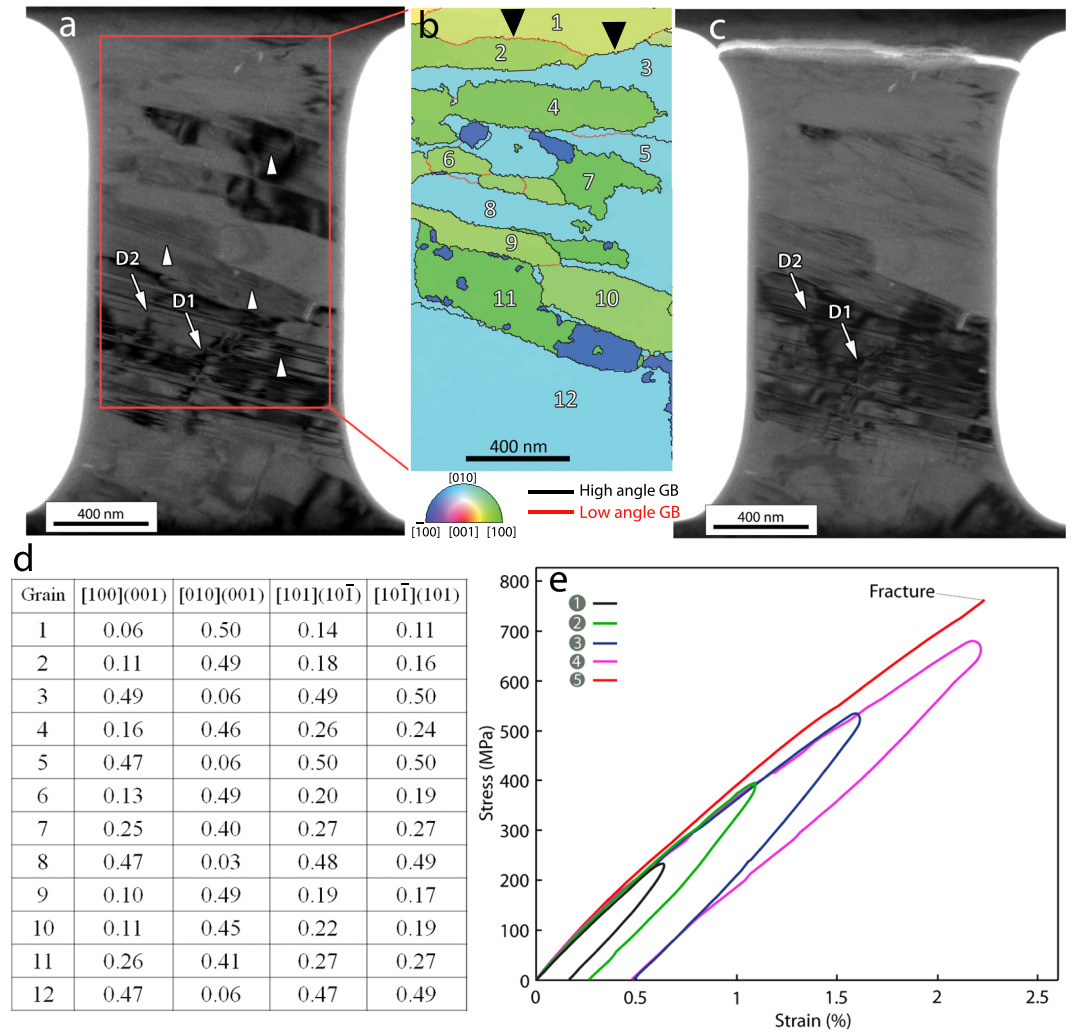
Grain	[100](001)	[010](001)	$[101](10\bar{1})$	$[10\bar{1}](101)$
1	0.06	0.50	0.14	0.11
2	0.11	0.49	0.18	0.16
3	0.49	0.06	0.49	0.50
4	0.16	0.46	0.26	0.24
5	0.47	0.06	0.50	0.50
6	0.13	0.49	0.20	0.19
7	0.25	0.40	0.27	0.27
8	0.47	0.03	0.48	0.49
9	0.10	0.49	0.19	0.17
10	0.11	0.45	0.22	0.19
11	0.26	0.41	0.27	0.27
12	0.47	0.06	0.47	0.49

Figure 2. Ant624-10-01 experiment. (a) Specimen mounted on the PTP device before deformation. White arrowheads indicate nanoscale planar defects. Two dislocations named D1 and D2 are indicated by white arrows. (b) Orientation map (210 × 370 pixels) obtained in the area delimited by the red rectangle in (a); inverse pole figure (IPF) along the direction normal to the figure plane. Low-angle (<15°) grain boundaries are drawn with red lines; high-angle grain boundaries are drawn with black lines. (c) Specimen after fracture in Cycle 5 in (e). (d) Schmid factors for the [100](001), [010](001), $[101](10\bar{1})$, and $[10\bar{1}](101)$ slip systems. (e) Engineering stress-strain curves corresponding to the successive five deformation cycles applied until fracture (always drawn with starting deformation set to 0).

reveals that several domains are well oriented for the activation of the [100](001), [010](001), $[101](10\bar{1})$, and $[10\bar{1}](101)$ slip systems (Figure 3e). Six deformation cycles have been performed under load control mode with a loading rate of 1 μN/s while imposing an increased maximum load after each cycle (Figure 3f). The apparent Young's modulus is found equal to 19.8 GPa, and the apparent Poisson ratio is equal to 0.22 (Table 1). Again, accumulation of plastic strain with increasing deformation cycles can be observed in Figure 3f. However, similar to Ant624-10-01 specimen, no dislocation movement was observed within the grains. Compared with specimen Ant624-10-01 analyzed in section 3.1, fracture (Figure 3d) occurred during the last sixth cycle at a relatively similar accumulated strain of 3.1% but at a lower applied stress of 319 MPa (Figure 3f). Fracture "partially" occurred along the GB indicated by a white arrow in Figures 3a and 3b, with a misorientation angle between 8° and 20°. Furthermore, careful analysis of TEM contrast revealed that GB sliding occurred before fracture along the GB indicated in Figures 3a and 3b.

Table 1
Elastic Properties of Antigorite Determined by the In Situ PTP Experiments

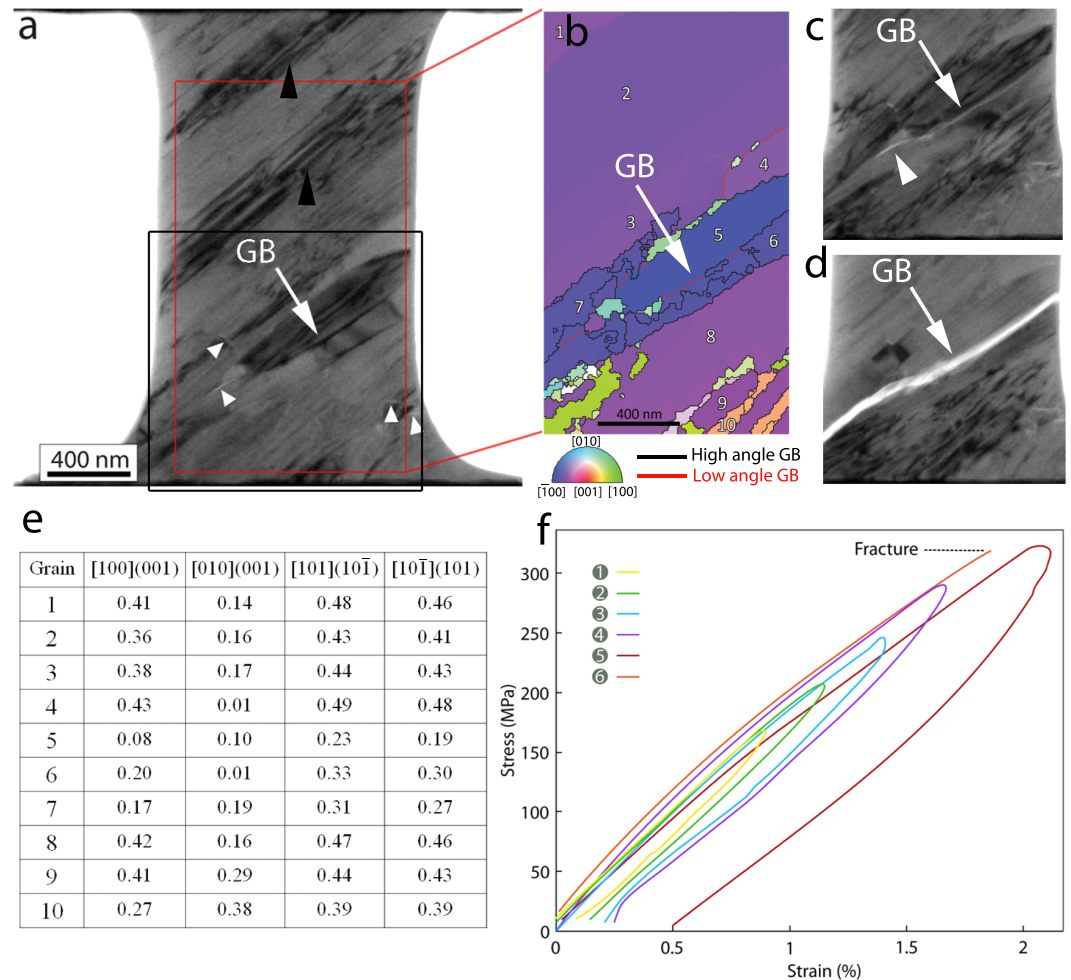| Specimen	Apparent Young's modulus (GPa)	Apparent Poisson ratio
Ant624-10-01	42.5	0.20
AntCU65-01	19.8	0.22
Ant624-10-02	30.6	0.21

Figure 3. In situ tensile test on the AntCU65-01 specimen. (a) TEM micrograph of the specimen before deformation. (b) Orientation map (270 × 460 pixels) obtained in the area delimited by the red rectangle in (a); IPF along the direction normal to the figure plane. Low-angle (<15°) grain boundaries are drawn with red lines; high-angle grain boundaries are drawn with black lines. (c) Area delimited by black square in (a) before sliding at 225 MPa in Cycle 5 in (f). Note the bright contrast at the grain boundary indicated by GB when compared to (a). (d) Same area after fracture at GB. (e) Schmid factors for the [100](001), [010](001), [101]($10\bar{1}$) and [$10\bar{1}$](101) slip systems. (f) Engineering stress-strain curves for the successive six deformation cycles applied until fracture.

Indeed, changes of diffraction contrast (from dark to white) along this GB can be clearly observed in Figure 3c during Cycle 5 at 225 MPa. This phenomenon initiates at the tip of the nanocrack connected to the same GB and indicated by white arrowhead in Figure 3c (see Movie AntCU65-01 at https://doi.org/10.5281/zenodo.3583135). Such a behavior was difficult to detect in the Ant624-10-01 specimen since the GB where fracture occurred was located in a region out of Bragg condition (Figure 2). It is also worth noting that in Figure 3f, Cycle 5 (in which GB sliding can be clearly observed) exhibits the highest permanent deformation compared to all the other cycles in the same figure. Again, the strain increases at the early stage of unloading due to activation of some creep mechanisms in Figure 3f, suggesting the activation of GB processes.

3.3. Ant624-10-02 Experiment (Influence of Loading Rate)

Figure 4a exhibits the engineering stress-strain curve corresponding to several loading cycles imposed on a uniaxial test specimen prepared from Antigorite624-10 (Figure 4b). Some preexisting nanocracks/voids can be observed at the GBs in this specimen (white arrows in Figure 4b). The objective here was to investigate the influence of the loading rate on the mechanical response and on the governing deformation mechanisms.
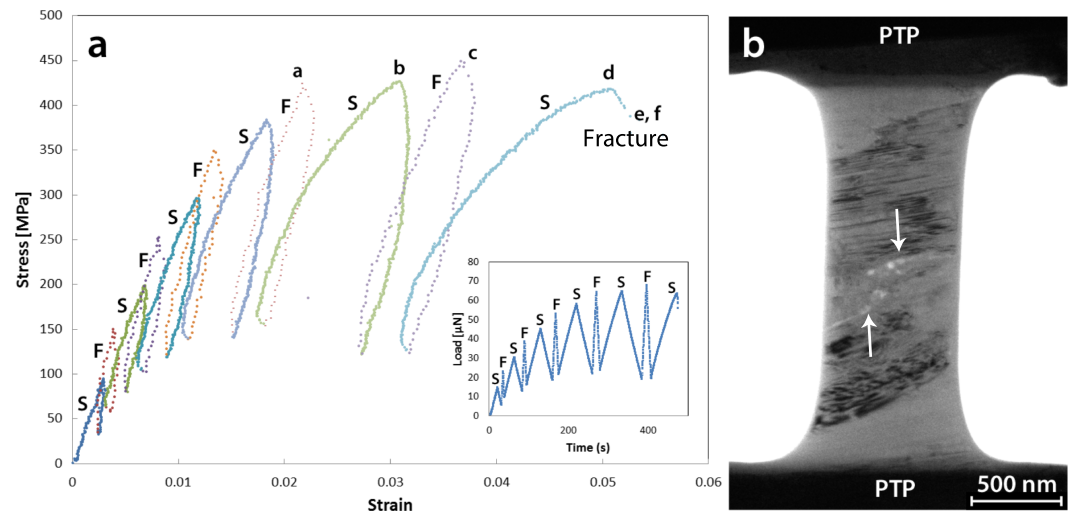
Figure 4. In situ tensile test on the Ant624-10-02 specimen showing the effect of loading rate on the tensile response. (a) Engineering stress-strain curves for the successive 11 deformation cycles applied until fracture. Changes of loading rate (alternating from 1 to 5 µN/s) are presented in the lower right inset. "S" and "F" refer to cycles with "slow" and "fast" loading rates, respectively. (b) BF-TEM image of the specimen mounted on the PTP device before deformation. Preexisting damages at GBs are indicated by white arrows.

Eleven loading cycles were performed by alternating the loading rate from 1 to 5 µN/s (inset in Figure 4a) and increasing the maximum load after each cycle. The apparent Young's modulus is here equal to 30.6 GPa with an apparent Poisson ratio equal to 0.21 (Table 1). Contrary to the previous specimens, the experiments were not stopped after each cycle. Figure 4a shows that, for cycles performed with similar loading rate, the permanent deformation increment increases cycle after cycle, in agreement with the previous experiments. There is a significant effect of the loading rate on the mechanical response. Indeed, it can be seen in Figure 4a that the plastic strain is higher (respectively lower) for the low (respectively high) loading rate involving also more (respectively less) creep deformation. This observation agrees with the GB sliding mechanism proposed in the previous sections as the main permanent deformation mechanism. The following TEM observations add extra evidences to this scenario. Figure 5 shows TEM snapshots selected at the positions a–f along the stress-strain response of Figure 4a. It demonstrates intense GB sliding along the GBs indicated by white arrowheads in the same figure (see also Movie Ant624-10-02 at https://doi.org/10.5281/zenodo.3583135). Figure 6 exhibits the evolution with increasing deformation of the transmitted beam intensity across the grain boundary GB$_F$ where failure ultimately occurred, as shown in Figure 5. It clearly shows a gradual increase of intensity at GB$_F$ from Figures 5a to 5f, which can be explained by the GB sliding mechanism illustrated in the right inset of the graph of Figure 6. The specimen fails under a stress equal to 387 MPa and 5.2% total accumulated strain. The high number of active GBs in Figure 5 can also explain the fact that the fracture strain here is significantly higher when compared with the previous specimens. The effect of electron beam irradiation on the tensile response has been excluded as a significant contributive mechanism (see supporting information).

4. Discussion

We present what is, to the best of our knowledge, the first characterization of the elastic (E and ν), and viscoplastic properties of antigorite from strain measurements performed in situ in a TEM during tensile tests. In terms of mechanical properties at low strains, the tests yield to Poisson ratio values from 0.2 to 0.22 (see Table 1), slightly lower, but which compare quite well to the value of 0.26 reported in the literature on bulk specimens (Bezacier et al., 2010, Brillouin scattering data; David et al., 2018, static compression data). For reasons clarified hereafter, we call this an "apparent" Poisson ratio. There are less data available in the literature concerning the Young's modulus. Most published values are provided for bulk modulus (K) or shear modulus (G). The Young's modulus can be deduced from those using the classical elasticity relation $E = 9KG/(3K + G)$. This leads to values significantly larger than ours (2 to 3 times). We compare, however,
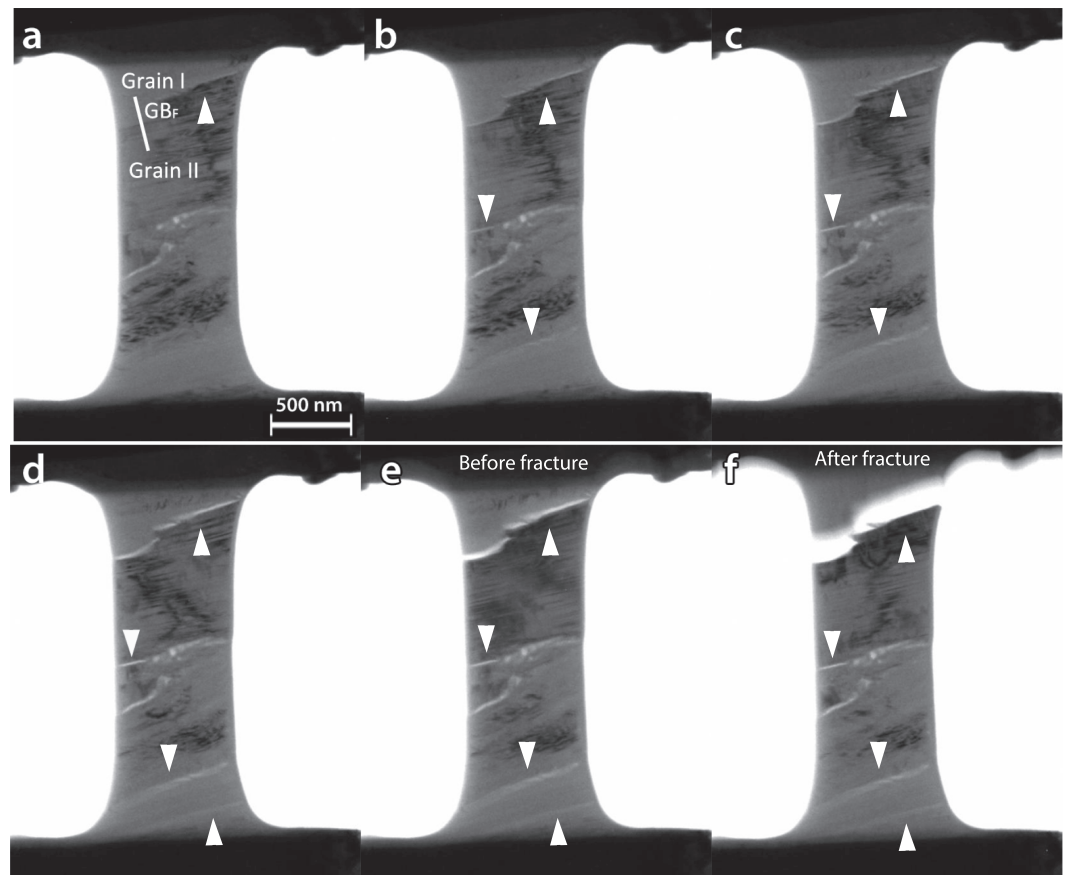
Figure 5. (a–f) In situ tensile test on the Ant624-10-02 specimen. Snapshots from the in situ TEM movie during deformation cycles in Figure 4a. Sliding GBs are indicated by white arrowheads.

mechanical properties evaluated in very different conditions. Bezacier et al. (2010) present data from Brillouin scattering measurements, David et al. (2018) performed triaxial compression tests, Hilairet et al. (2006) determined equations of state from diamond anvil cell experiments, while Capitani and Stixrude (2012) and Mookherjee and Capitani (2011) performed density functional theory calculations of static compression. Our experiments are the only ones where the modulus is measured from uniaxial tensile tests on specimens with very small sizes and containing a very small number of grains with a limited number of orientations. Hence, our values should be compared to single crystal data rather than to polycrystal averages. Depending on the tensile direction, the Young's modulus of antigorite single crystals ranges from 44 to 185 GPa (calculations performed from the single crystal elastic constants of Bezacier et al., 2010). Still our measured values appear significantly lower which suggests that what may appear as an elastic portion of the stress-strain curves does not correspond to a purely elastic behavior. Some anelasticity is activated very early (below 150 MPa) that results in lower Young's modulus values, hence named "apparent" Young's modulus. This observation should be compared to the recent report of Burnley and Kaboli (2019) on San Carlos olivine aggregates who found low values of apparent Young's modulus resulting from inelastic behavior at low strain. Following several earlier theoretical studies (e.g., Ghahremani, 1980; Zener, 1941), Burnley and Kaboli propose that the reduction of Young's modulus results from viscous relaxation processes at the grain boundaries. The low values of Young's modulus measured in our experiments are thus consistent with observation of GB sliding and suggest that this mechanism becomes active and contributes to anelasticity of the samples at small loads, even before GB motions are observed on the micrographs.

The mechanical behavior of antigorite has already been investigated at room temperature on bulk specimens by Escartin et al. (1997) and David et al. (2018) with a view to characterize the brittle-ductile transition in serpentinites. Escartin et al. (1997) used a gas confining medium and a solid confining medium (Griggs-type) apparatus. David et al. (2018) conducted deformation experiments in an oil medium triaxial apparatus.
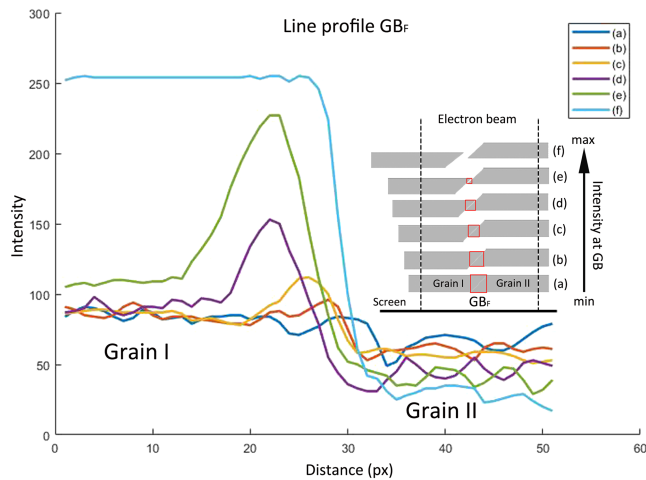
Figure 6. Evolution with increasing deformation of the transmitted beam intensity across the grain boundary GB_F (white line at GB_F in Figure 5a) at which failure ultimately occurred in specimen Ant624-10-02. The curves (a to f) refer to the corresponding snapshots in Figures 5a–5f. The gradual increase of the maximum intensity in the graph can be explained by the grain boundary sliding mechanism as shown in the right inset. Indeed, the interaction area (delimited by the red squares) between the parallel electron beam (black vertical parallel dash lines) and the GB gradually decreases with increasing deformation leading to a gradual increase of the maximum intensity transmitted at the GB. The maximum intensity shown by Curve f belongs to the transmitted beam without the presence of the sample, hence after fracture opening (Figure 5f).

Although our experiments are conducted under very different conditions (small specimen size, no confining pressure), the mechanical data are very consistent. In particular, the cyclic loading experiments of David et al. (2018), see their Figures 4 and 5, compare very well to ours in terms of yield stress and maximum stress to failure. The added value permitted by our experiments is to observe in situ the evolution of the microstructure in direct relationship with the mechanical response. Our observations show the following under the specific conditions of the present experiments:

- *Antigorite does not exhibit a purely elastic-brittle behavior.* Although our specimens are very small, they are not free of defects and damage. In our experiments, no confining pressure is applied to prevent brittle failure. On the contrary, the specimen environment is the vacuum of the microscope column. However, the specimens did not fail in the elastic regime, and significant plastic strain (several percent) was accumulated before failure. Cycling loading performed on Ant624-10-02 specimen shows that the accumulated plastic strain does not result from opening of cracks or pores (which would lead to significant variation of the elastic stiffness from cycle to cycle) but from a GB-related process. The sensitivity to the applied loading rate demonstrates that the accumulation of irreversible strain results from a time-dependent mechanism which is found to operate at small loads (below 150 MPa, as can be seen from the low values of the apparent Young's modulus).

- *There is no dislocation activity.* The plastic mechanism observed is not linked to dislocation glide. Very few dislocations were present in the specimens before load was applied (Figure 2a). We did not see them moving (Figure 2c), although they were subjected to significant resolved shear stress (See Schmid factors in Figure 2d). More generally, by determining the local orientations using ACOM-TEM, we have checked that several domains were conveniently oriented for activating plastic slip as a response of the applied tensile loading. The absence of dislocation activity cannot be attributed to unfavorable orientations corresponding to very small resolved shear stresses. In such small specimens, dislocations gliding and reaching the surfaces leave ledges which can be observed (see Figure 4 in Samaee et al., 2018). We do not see the formation of such ledges in our specimens. From Ant624-10-02, one can place a lower bound for dislocation activity in antigorite at room temperature at 390 MPa. As already proposed by several authors, we think that this resistance to plastic shear must be related to the corrugation of the basal plane in antigorite. Indeed, the periodic reversal of tetrahedral sheets involves the formation of covalent Si-O-Si bonds. Contrary to other sheet silicates, there exists no plane in antigorite where plastic shear can occur without breaking those bonds.

- *Viscoplasticity is achieved by grain boundary sliding.* As indicated above, several evidences point to the role played by grain boundaries in the viscoplastic behavior of the antigorite specimens. The first one is of course the absence of evidence for any active intragranular mechanism. Second, we observe that failure always occurred ultimately along preexisting boundaries. Finally, Figure 5 and quantification in Figure 6 very clearly show the contrast evolving at the boundaries and becoming progressively brighter as the boundary region becomes thinner. This is a direct evidence of a GB sliding process. Failure does not result by opening of a crack in mode I along the boundary since in that case, the contrast would jump abruptly to the maximum value of the background outside the specimen. From a kinematic point of view, the GB sliding process is similar to a mixed mode II or III crack propagation, except that it localizes at grain boundaries. We show also that this mechanism is rate dependent, probably as a result of thermally activated processes. This is evidenced by the change of plastic strain with loading rate but also by the significant forward creep observed during unloading. GB sliding appears to be very easy to activate since it leads to an anelastic response very early during loading responsible for the low values of the apparent Young's modulus. We can estimate that the threshold resolved shear stress for activating GB sliding is below 150 MPa assuming that the most activated grain boundaries are oriented near 45° from the main loading direction.

- *Failure occurs at GBs.* All our experiments were conducted until specimen failure. Failure occurs when cohesion is lost at a sliding boundary (see Figures 5 and 6). The ultimate strain is reached rapidly in these experiments since the specimens are very thin. This, plus the fact that the number of boundaries varies, explains that failure can occur at different values of stresses or strains. It is worth noting that, since the observed plastic strain results from localization at grain boundaries, failure occurs at places where the local shear strain is much larger than the average values measured from Figures 2–4. Care must be taken in applying our results to bulk specimens. Here due to the small size of the specimens, sliding can operate rather homogeneously along the boundary with no difficulty for accommodating the finite displacement except for the bending of the specimen. This is not the case in bulk specimens where GB sliding is usually heterogeneous along the interface and leads to strain incompatibilities, mostly at triple junctions (Bourcier et al., 2013). It appears necessary to develop plasticity models of phyllosilicate aggregates to understand how GB sliding can influence mechanical properties of bulk specimens.

In analyzing their experiments, Escartin et al. (1997) and David et al. (2018) proposed a mechanical behavior dominated by "mixed mode II + mode III" shear microcracking. Our observations are fully compatible with this interpretation. Our in situ observations bring, however, more information and show that "microcracking" does not occur randomly or inside grains along the basal plane but that this mechanism is localized along grain boundaries. Wassmann et al. (2011) studied the deformed microstructures from serpentinites in exhumed high-pressure metamorphic rocks exposed in the Zermatt-Saas zone, Western Alps. They concluded that there was no evidence for significant deformation in the field of dislocation creep, although they do not exclude a possible contribution of basal glide in antigorite. Our observation does indeed not support the hypothesis of easy dislocation glide in antigorite at least at room temperature. The influence of temperature on dislocation glide in antigorite will need to be studied. Instead, Wassmann et al. (2011) found indications that dissolution precipitation creep is the predominant deformation mechanism (a hypothesis also proposed by Andreani et al., 2005, on different serpentinites). This is certainly not a mechanism that we can consider during in situ deformation experiments in a TEM. However, we want to point out that GB sliding, especially in very anisotropic structures like phyllosilicates, is very likely to induce damage, especially at triple junctions, and hence to enhance permeability at large strains. This permeability might in turn help activating dissolution precipitation creep.

The main message from the present study is to highlight the potential role of grain boundaries on the mechanical properties of antigorite. On a more general level, the structure of grain boundaries in phyllosilicates has received relatively little attention. In chlorite, the structure of low-angle tilt boundaries has been imaged by High Resolution Transmission Electron Microscopy (Kogure & Murakami, 1998) showing well-organized interfaces except in periodic triangular units which may contain amorphous materials. In slates, several types of boundaries classified as coherent, semicoherent, and incoherent have been identified (Bons et al., 1990). Incoherent boundaries have been found to be much more sensitive to beam damage in the TEM. In chlorite from a thrust fault, Buatier et al. (2012) present evidence of damaged high-angle grain boundaries. However, Wirth (1987) reported evidence for well-organized boundaries in biotite (including an asymmetrical 37° tilt boundary) and chlorite with lattice fringes coming into contact at the boundary. Despite very strong geometrical constraints from the crystal chemistry, some well-organized grain boundaries can form, at least for some orientation relationships. However, the information available is too scarce to assess how anisotropic the structural organization of the grain boundaries and their cohesion are. One must also consider that phyllosilicates also often exhibit strong shape preferred orientations of grains. Sintubin et al. (1995) discussed the implications of platy grain morphologies on the development of crystal preferred orientations (incidentally, this might be taken as an indication of dislocation creep processes). This might give rise to a selection of misorientations between grains with a possible higher representation of low-angle grain boundaries. More work is needed to better understand the structures and properties of grain boundaries in antigorite and more generally in phyllosilicates.

5. Conclusion

The present study involving in situ tensile deformation experiments in a transmission electron microscope emphasizes the prominent role played by GB sliding in the plastic behavior of antigorite at room temperature. This mechanism has not been very much considered so far, but its occurrence seems fully consistent

with previous studies on antigorite at room temperature reported by Escartin et al. (1997) and David et al. (2018). The structure and properties of grain boundaries are not well known in complex structures like phyllosilicates. Our study calls for more work in this direction in order to describe properly the mechanical behavior of these materials.

References

Amiguet, E., Reynard, B., Caracas, R., Van De Moortèle, B., Hilairet, N., & Wang, Y. (2012). Creep of phyllosilicates at the onset of plate tectonics. *Earth and Planetary Science Letters*, *345-348*, 142–150. https://doi.org/10.1016/j.epsl.2012.06.033

Amiguet, E., Van De Moortèle, B., Cordier, P., Hilairet, N., & Reynard, B. (2014). Deformation mechanisms and rheology of serpentines in experiments and in nature. *Journal of Geophysical Research: Solid Earth*, *119*, 4640–4655. https://doi.org/10.1002/2013JB010791

Andreani, M., Boullier, A. M., & Gratier, J. P. (2005). Development of schistosity by dissolution–crystallization in a Californian serpentinite gouge. *Journal of Structural Geology*, *27*, 2256–2267.

Angiboust, S., Langdon, R., Agard, P., Waters, D., & Chopin, C. (2011). Eclogitization of the Monviso ophiolite (W. Alps) and implications on subduction dynamics. *Journal of Metamorphic Petrology*, *30*(1), 37–61. https://doi.org/10.1111/j.1525-1314.2011.00951.x

Aumento, F., & Loubat, H. (1971). The Mid-Atlantic Ridge near 45°N. XVI. Serpentinized ultramafic intrusions. *Canadian Journal of Earth Sciences*, *8*(6), 631–663. https://doi.org/10.1139/e71-062

Auzende, A. L., Devouard, B., Guillot, S., Daniel, I., Baronnet, A., & Lardeaux, J. M. (2002). Serpentinites from Central Cuba: Petrology and HRTEM study. *European Journal of Mineralogy*, *14*(5), 905–914. https://dx.doi.org/10.1127/0935-1221/2002/0014-0905

Auzende, A. L., Escartin, J., Walte, N. P., Guillot, S., Hirth, G., & Frost, D. J. (2015). Deformation mechanisms of antigorite serpentinite at subduction zone conditions determined from experimentally and naturally deformed rocks. *Earth and Planetary Science Letters*, *411*, 229–240. https://doi.org/10.1016/j.epsl.2014.11.053

Auzende, A. L., Guillot, S., Devouard, B., & Baronnet, A. (2006). Serpentinites in an Alpine convergent setting: Effects of metamorphic grade and deformation on microstructures. *European Journal of Mineralogy*, *18*(1), 21–33. https://doi.org/10.1127/0935-1221/2006/0018-0021

Bezacier, L., Reynard, B., Bass, J., Sanchez-Valle, C., & Van de Moortèle, B. (2010). Elasticity of antigorite, seismic detection of serpentinites, and anisotropy in subduction zones. *Earth and Planetary Science Letters*, *289*, 198–208.

Bons, A. J., Drury, M. R., Schryvers, D., & Zwart, H. J. (1990). The nature of grain boundaries in slates, implications for mass transport processes during low temperature metamorphism. *Physics and Chemistry of Minerals*, *17*, 402–408.

Boudier, F., Baronnet, A., & Mainprice, D. (2010). Serpentine mineral replacements of natural olivine and their seismic implications: Oceanic lizardite versus subduction-related antigorite. *Journal of Petrology*, *51*, 495–512.

Bourcier, M., Bornert, M., Dimanov, A., Héripré, E., & Raphanel, J. L. (2013). Multiscale experimental investigation of crystal plasticity and grain boundary sliding in synthetic halite using digital image correlation. *Journal of Geophysical Research: Solid Earth*, *118*, 511–526. https://doi.org/10.1002/jgrb.50065

Brownlee, S. J., Hacker, B. R., Harlow, G. E., & Seward, G. (2013). Seismic signatures of a hydrated mantle wedge from antigorite crystal-preferred orientation (CPO). *Earth and Planetary Science Letters*, *375*, 395–407. https://doi.org/10.1016/j.epsl.2013.06.003

Buatier, M., Lacroix, B., Labaume, P., Moutarlier, V., Charpentier, D., Sizun, J. P., & Travé, A. (2012). Microtextural investigation (SEM and TEM study) of phyllosilicates in a major thrust fault zone (Monte Perdido, southern Pyrenees): Impact on fault reactivation. *Swiss Journal of Geosciences*, *105*(2), 313–324. https://doi.org/10.1007/s00015-012-0098-0

Burnley, P. C., & Kaboli, S. (2019). Elastic plastic self-consistent (EPSC) modeling of San Carlos olivine deformed in a D-DIA apparatus. *American Mineralogist*, *104*(2), 276–281. https://doi.org/10.2138/am-2019-6666

Capitani, G. C., & Merlini, M. (2004). The modulated crystal structure of antigorite: The $m = 17$ polysome. *American Mineralogist*, *89*, 147–158.

Capitani, G. C., & Stixrude, L. (2012). A first-principle investigation of antigorite up to 30 GPa: Structural behavior under compression. *American Mineralogist*, *97*, 1177–1186.

Chernak, L. J., & Hirth, G. (2010). Deformation of antigorite serpentinite at high temperature and pressure. *Earth and Planetary Science Letters*, *296*, 23–33.

Chisholm, C., Bei, H., Lowry, M. B., Oh, J., Syed Asif, S. A., Warren, O. L., et al. (2012). Dislocation starvation and exhaustion hardening in Mo alloy nanofibers. *Acta Materialia*, *60*, 2258–2264. https://doi.org/10.1016/j.actamat.2011.12.027

David, E. C., Brantut, N., Hansen, L. N., & Mitchell, T. M. (2018). Absence of stress-induced anisotropy during brittle deformation in antigorite serpentinite. *Journal of Geophysical Research: Solid Earth*, *123*, 10,616–10,644. https://doi.org/10.1029/2018JB016255

Escartin, J., Hirth, G., & Evans, B. (1997). Non-dilatant brittle deformation of serpentinites: Implications for Mohr-Coulomb theory and the strength of faults. *Journal of Geophysical Research*, *102*(B2), 2897–2913.

Ghahremani, F. (1980). Effect of grain boundary sliding on anelasticity of polycrystals. *International Journal of Solids and Structures*, *16*(9), 825–845. https://doi.org/10.1016/0020-7683(80)90052-9

Guillot, S., & Hattori, K. (2013). Serpentinites: Essential roles in geodynamics, arc volcanism, sustainable development, and the origin of life. *Elements*, *9*(2), 95–98.

Guillot, S., Schwartz, S., Reynard, B., Agard, P., & Prigent, C. (2015). Tectonic significance of serpentinites. *Tectonophysics*, *646*, 1–19. https://doi.org/10.1016/j.tecto.2015.01.020

Hilairet, N., Daniel, I., & Reynard, B. (2006). P–V equations of state and the relative stabilities of serpentine varieties. *Physics and Chemistry of Minerals*, *33*(8-9), 629–637. https://doi.org/10.1007/s00269-006-0111-0

Hilairet, N., Reynard, B., Wang, Y. B., Daniel, I., Merkel, S., Nishiyama, N., & Petitgirard, S. (2007). High-pressure creep of serpentine, interseismic deformation, and initiation of subduction. *Science*, *318*(5858), 1910–1913. https://doi.org/10.1126/science.1148494

Idrissi, H., Bollinger, C., Boioli, F., Schryvers, D., & Cordier, P. (2016). Low temperature plasticity of olivine revisited with in situ TEM nanomechanical testing. *Science Advances*, *2*, e1501671 (1-6). https://doi.org/10.1126/sciadv.1501671

Katayama, I. (2009). Thin anisotropic layer in the mantle wedge beneath northeast Japan. *Geology*, *37*(3), 211–214.

Kogure, T., & Murakami, T. (1998). Structure and formation mechanism of low-angle grain boundary in chlorite. *American Mineralogist*, *83*, 358–364.

Morales, L. F. G., Mainprice, D., & Boudier, F. (2013). The influence of hydrous phases on the microstructure and seismic properties of a hydrated mantle rock. *Tectonophysics*, *594*, 103–117.

Mookherjee, M., & Capitani, G. C. (2011). Trench parallel anisotropy and large delay times: Elasticity and anisotropy of antigorite at high pressures. *Geophysical Research Letters*, *38*, L09315. https://doi.org/10.1029/2011GL047160

Padrón-Navarta, J. A., Tommasi, A., Garrido, C. J., & Sánchez-Vizcaíno, V. L. (2012). Plastic deformation and development of antigorite crystal preferred orientation in high-pressure serpentinites. *Earth and Planetary Science Letters*, *349–350*, 75–86.

Plümper, O., King, H. E., Vollmer, C., Ramasse, Q., Jung, H., & Austrheim, H. (2012). The legacy of crystal-plastic deformation in olivine: High-diffusivity pathways during serpentinization. *Contributions to Mineralogy and Petrology*, *163*(4), 701–724.

Raleigh, C. B., & Paterson, M. S. (1965). Experimental deformation of serpentinite and its tectonic implications. *Journal of Geophysical Research*, *70*, 3965–3985.

Reynard, B. (2013). Serpentine in active subduction zones. *Lithos*, *178*, 171–185.

Samaee, V., Gatti, R., Devincre, B., Pardoen, T., Schryvers, D., & Idrissi, H. (2018). Dislocation driven nanosample plasticity: New insights from quantitative in-situ TEM tensile testing. *Scientific Reports*, *8*(1), 12012 (1-11). https://doi.org/10.1038/s41598-018-30639-8

Scamberulli, M., Müntener, O., Hermann, J., Piccardo, G. B., & Trommsdorff, V. (1995). Subduction of water in the mantle: History of an Alpine peridotite. *Geology*, *23*, 459–462.

Soda, Y., & Wenk, H. R. (2014). Antigorite crystallographic preferred orientations in serpentinites from Japan. *Tectonophysics*, *615–616*, 199–212.

Ulmer, P., & Trommsdorff, V. (1995). Serpentine stability to mantle depths and subduction-related magmatism. *Science*, *268*(5212), 858–861. https://doi.org/10.1126/science.268.5212.858

Wassmann, S., Stöckhert, B., & Trepmann, C. A. (2011). Dissolution precipitation creep versus crystalline plasticity in high pressure metamorphic serpentinites. *Geological Society, London, Special Publications*, *360*, 129–149. https://doi.org/10.1144/SP360.8

Sintubin, M., Wenk, H. R., & Phillips, D. S. (1995). Texture development in platy materials: Comparison of Bi2223 aggregates with phyllosilicate fabrics. *Materials Science and Engineering*, *A202*(157), 171.

Wirth, R. (1987). High-angle grain boundaries in sheet silicates (biotite/chlorite): A TEM study. In J. A. Pask & A. G. Evans (Eds.), *Ceramic Microstructures'86 Role of Interfaces* (Vol. 21, pp. 249–253). New York and London: Plenum Press.

Zener, C. (1941). Theory of the elasticity of polycrystals with viscous grain boundaries. *Physical Review*, *60*, 906–908. https://doi.org/10.1103/PhysRev.60.906